FRONTIERS OF PHYSICS

RESEARCH ARTICLE
Volume 22 / Issue 4 / 044201 / 2027

Wavelength-selective dual-channel coupling transistor for neuromorphic vision and In-sensor logic

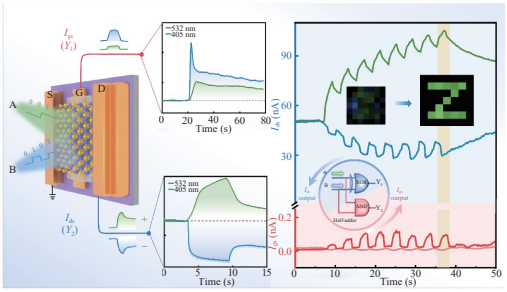
Yurong Jiang†, Jianing Zhang, Suicai Zhang, Xuan Qin, Leiming Yu, Xueping Li, Xiaohui Song, Congxin Xia‡

1 School of Physics, Henan Key Laboratory of Advanced Semiconductor & Functional Device Integration, Henan Normal University, Xinxiang 453007, China
2 College of Electronic and Electrical Engineering, Henan Normal University, Xinxiang 453007, China
Corresponding authors. E-mail: †jiangyurong@htu.edu.cn, ‡xiacongxin@htu.edu.cn
Received June 20, 2026; accepted August 18, 2026

© Higher Education Press 2027

ABSTRACT

Most existing hardware based on the von Neumann architecture inherently features a single readout, which limits multifunctional capabilities in advanced computing systems. Here, we report a wavelength-selective dual-channel coupling transistor based on an MoS_2 channel and ferro-photoactive $CuInP_2S_6$ (CIPS) gate, which simultaneously generates horizontal source–drain (I_{ds}) and vertical gate-source (I_{gs}) dual readouts under optical illumination. Under 532 nm and 405 nm illumination, the device exhibits wavelength-dependent synaptic response polarity: the I_{ds} current mimics the center-excitatory pathway of bipolar cells, while the I_{gs} current mimics the surround-inhibitory pathway of horizontal cells, enabling bio-inspired in-sensor neuromorphic perception. Moreover, the wavelength-selective dual readouts enable reconfigurable XOR and AND optical logic operations within a single device, allowing it to function as an all-optical half-adder. This reduces the component count by 91.7% compared with CMOS-based circuits. Our device integrates sensing, neuromorphic preprocessing, and arithmetic logic within a single hardware unit, paving the pathway toward compact, energy-efficient vision systems.



Keywords ferro-photoactive gate, dual-readout, retina-neuromorphic, half-adder, dual-channel coupling

1 Introduction

The von Neumann architecture inherently suffers from energy inefficiency and latency due to the physical separation of sensors, memory, and processors [1–4], a bottleneck that is particularly prominent in visual information processing [5–9]. Biological retinas address this challenge through a parallel "center-excitation and periphery-inhibition" processing mechanism [10–12], accomplishing dynamic range compression and feature extraction with merely microwatt-scale power consumption. This provides an ideal blueprint for neuromorphic device design.

Two-dimensional (2D) materials, characterized by atomic thickness, tunable bandgaps, and strong light-matter interactions, have emerged as promising platforms for bio-inspired optoelectronic devices [13–16]. In the field of visual simulation, WSe_2-based bifurcated floating-gate device arrays have successfully emulated retinal functions [17], while MoS_2 exhibits advantages in dynamic visual adaptability advantages — such as alcohol-doped MoS_2 photonic synapses that simulate human

https://doi.org/10.15302/frontphys.2027.044201

eye adaptation mechanisms [18], and Fe_7S_8@MoS_2 heterostructures that achieve 92% recognition accuracy under low-light conditions [19]. In addition, a $ReS_2/CuInP_2S_6$ heterostructure realizes the emulation of multimodal synapses by leveraging the polarization switching of CIPS and the laser-induced carrier relaxation process in ReS_2 [20]. Moreover, an optoelectronic device based on a multilayer graphene/$CuInP_2S_6$/Au structure achieves visual perception, processing, and memory functions through photoelectrical cooperative modulation [21].

In addition, as a core component of arithmetic logic units, significant progress has been made in miniaturizing such logic elements using 2D materials — demonstrating transistors capable of XOR or AND operations, such as monolayer WSe_2 homojunction split-gate transistors [25], 2-transistor implementations based on dual-ferroelectric-gate $MoS_2/MoTe_2$ hetero-integration [26], and 2T2R structures leveraging 2D WSe_2/MoS_2 heterostructures [27]. However, these logic devices are typically developed in isolation from sensory components [22–24]. Most reported 2D optoelectronic synapses only perform retinal neuromorphic preprocessing without embedded logic functions, while standalone optical logic transistors require separate sensor units for signal pretreatment. Our wavelength-selective dual-channel coupling mechanism overcomes this functional segregation within a single MoS_2/CIPS heterostructure device.

Here, we materialize this vision by introducing a ferro-photoactive CIPS gate into a MoS_2 transistor, demonstrating wavelength-selective dual-channel coupling between I_{ds} and I_{gs}, wherein a single optical input elicits two distinct, antagonistic outputs, integrating bio-inspired preprocessing and logic capabilities into one single device. The I_{ds} mimics the bipolar cell's center-excitatory response, while I_{gs} mimics the horizontal cell's surround-inhibitory feedback, enabling the device to perform retina-like, in-sensor neuromorphic computing for real-time image enhancement. More importantly, we exploit the wavelength-dependent synergism and antagonism between these two channels to directly implement reconfigurable optical logic gates (XOR and AND), allowing a single device to function as an optical half-adder, a fundamental arithmetic unit. This work provides a tangible hardware blueprint for next-generation vision systems that are not only "smart" in perception but also capable of primitive decision-making at the very point of sensing, paving the way to overcome the von Neumann bottleneck in visual information processing.

2 Characterization and measurements

All few-layered $CuInP_2S_6$ and MoS_2 flakes were exfoliated from commercially available bulk crystals (purchased from Shanghai Onway Technology Co., Ltd.). The device is fabricated via an ultraviolet maskless lithography machine (TuoTuo Technology, UV Litho-ACA). The morphology of the thin film was measured using an atomic force microscope (AFM, Bruker Dimension Icon). UV-Vis absorption spectra were measured on a PerkinElmer Lambda 1050 spectrometer. Electrical measurements were conducted using an Agilent B1500A semiconductor parameter analyzer.

3 Results and discussion

The direct pathway and lateral pathway in the biological retina constitute the core mechanism of parallel visual signal processing, and this neural circuit is composed of photoreceptor cells (rods/cones cells), horizontal cells, and bipolar cells, which collectively enable efficient encoding and preprocessing of optical information collectively [28–30]. As shown in Fig. 1(a), in the center-surround receptive field in biological vision, horizontal cells act as key inhibitory interneurons in the outer retinal network, laterally connecting multiple photoreceptors and bipolar cells. Through γ-aminobutyric acid (GABA)-ergic inhibitory neurotransmission, this feedback mechanism ensures that bipolar cells simultaneously integrate direct central inputs and modulated peripheral inputs, establishing antagonistic center-surround receptive fields [31–34]. Inspired by this structure, we design a dual-channel output phototransistor based on MoS_2 channel and ferro-photoactive CIPS gate dielectric [Fig. 1(b)]. Schematic diagrams, an optical image, and an atomic force microscopy (AFM) image of the device are presented in Figs. S1(a–c) (Supporting Information). The thicknesses of the CIPS and MoS_2 films are approximately 50.4 nm and 5.9 nm, respectively. Figure S1(d) shows the Raman spectra of CIPS and MoS_2, whose characteristic peaks are consistent with those reported in the literature [35, 36]. Because the CIPS layer combines high-κ gate control capability (Fig. S2) with moderate bandgap characteristics, it can simultaneously output the main channel current I_{ds} (Y_1) and the light-induced gate current I_{gs} (Y_2) when stimulated by different wavelengths (532 nm and 405 nm). Here, "dual output" refers to the simultaneous readout of I_{ds} and I_{gs}, while "dual-channel coupling" describes the modulation of the horizontal MoS_2 channel current by photoinduced carrier transport through the vertical CIPS/MoS_2 path. As shown in Fig. 1(b), the resulting electrical response mimics the synaptic transmission and modulation processes of neurons after receiving neurotransmitters. The horizontal channel (Y_1) emulates the direct signal transmission of bipolar cells, while the vertical channel (Y_2) reproduces the lateral inhibition mediated by horizontal cells, thereby replicating the "center-surround" antagonistic visual information processing mechanism of the retina.

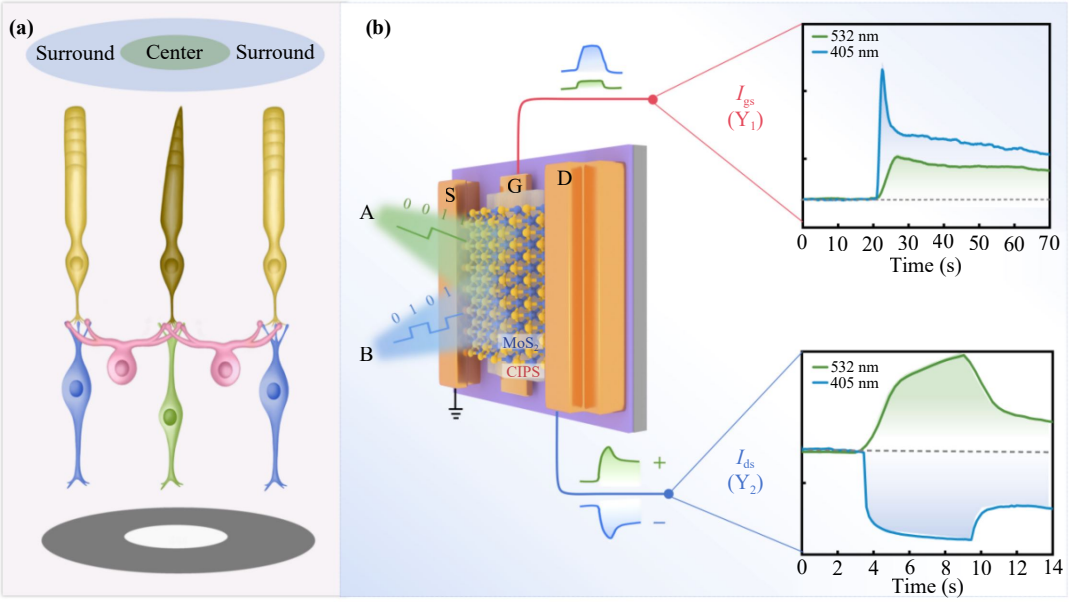


Fig. 1 Device architecture and bio-inspired retinal analogy. **(a)** Schematic illustration of the center-surround receptive field in biological vision. **(b)** Single device architecture with dual-readout channel.

This design provides an attractive insight into constructing a compact and efficient neuromorphic computing system. Under a negative gate voltage ($V_{gs} < 0$), the spectral response curves of the transistor all exhibit positive current changes. In contrast, when $V_{gs} > 0$, the device exhibits significant wavelength selectivity, 532 nm light irradiation enhances the current, while 405 nm light irradiation causes current attenuation [Fig. 2(a)]. To systematically investigate the photoresponse, we measured the I_{ds}–V_{gs} transfer characteristic curves under different irradiation conditions [Fig. 2(b)]. The observed counterclockwise hysteresis is mainly attributed to the polarization-induced electrostatic modulation of the MoS_2 channel by the ferroelectric CIPS gate. The curves show that the I_{ds} output exhibits typical n-type semiconductor behavior, with an on/off ratio of up to 10^6. Meanwhile, the curves demonstrate a significant wavelength-gate voltage synergistic effect. Under positive gate voltage and 532 nm light irradiation, long-wavelength photons primarily excite electron transport in the horizontal channel of MoS_2, leading to an increase in I_{ds}. Under 405 nm light irradiation, short-wavelength photons simultaneously activate the vertical channel modulated by the CIPS layer, generating a significant I_{gs} output [Fig. 2(c)]. In addition, the output curves of the photosensor were measured and are shown in Fig. S3, demonstrating excellent gate control capability.

Notably, the subthreshold characteristics extracted from Fig. 2(b) show that the minimum subthreshold swing (SS) is 50 mV·dec^{-1} [Fig. 2(d)], and that I_{ds} remains stable over four orders of magnitude, both of which reflect the device's low power consumption and excellent switching performance. After fabricating a MoS_2/h-BN photosensor by replacing CIPS with h-BN, we found that its SS was significantly higher than that of the MoS_2/CIPS photosensor (Fig. S4). This difference indicates that the excellent performance originates from the negative capacitance effect of the CIPS ferroelectric gate, which enables it to break through the 60 mV·dec^{-1} thermionic limit through internal amplification of the gate voltage [37–39]. The expression for SS is as follows:

$$SS = \frac{\mathrm{d}V_{gs}}{\mathrm{d}\left(\log_{10} I_{ds}\right)} = \frac{\mathrm{d}V_{gs}}{\mathrm{d}\psi_s} \times \frac{\mathrm{d}\psi_s}{\mathrm{d}\left(\log_{10} I_{ds}\right)} = m \times n, \quad (1)$$

where ψ_s is the surface potential.

By measuring the ultraviolet-visible (UV-Vis) absorption spectrum [Fig. 2(e)], it can be observed that MoS_2 exhibits strong absorption in the 405–532 nm wavelength range, while CIPS has a sharp absorption edge at ≈ 450 nm and weak absorption in the long-wavelength region. In the wavelength range of 450–800 nm, the lower absorbance of the CIPS/MoS_2 overlapping region is mainly attributed to the weak absorption of CIPS and the additional reflection and scattering losses introduced by the stacked heterostructure.

This spectral difference between CIPS and MoS_2 stems from their distinct band structures [Fig. 2(f)]. The electron affinities of CIPS and multilayer MoS_2 were taken as approximately 3.7 and 4.3 eV, respectively, based on previous reports [40, 41]. The optical bandgap of CIPS was determined to be approximately 2.9 eV from the UV-Vis absorption spectrum and Tauc analysis shown in Fig. S5, whereas the approximately 1.2 eV

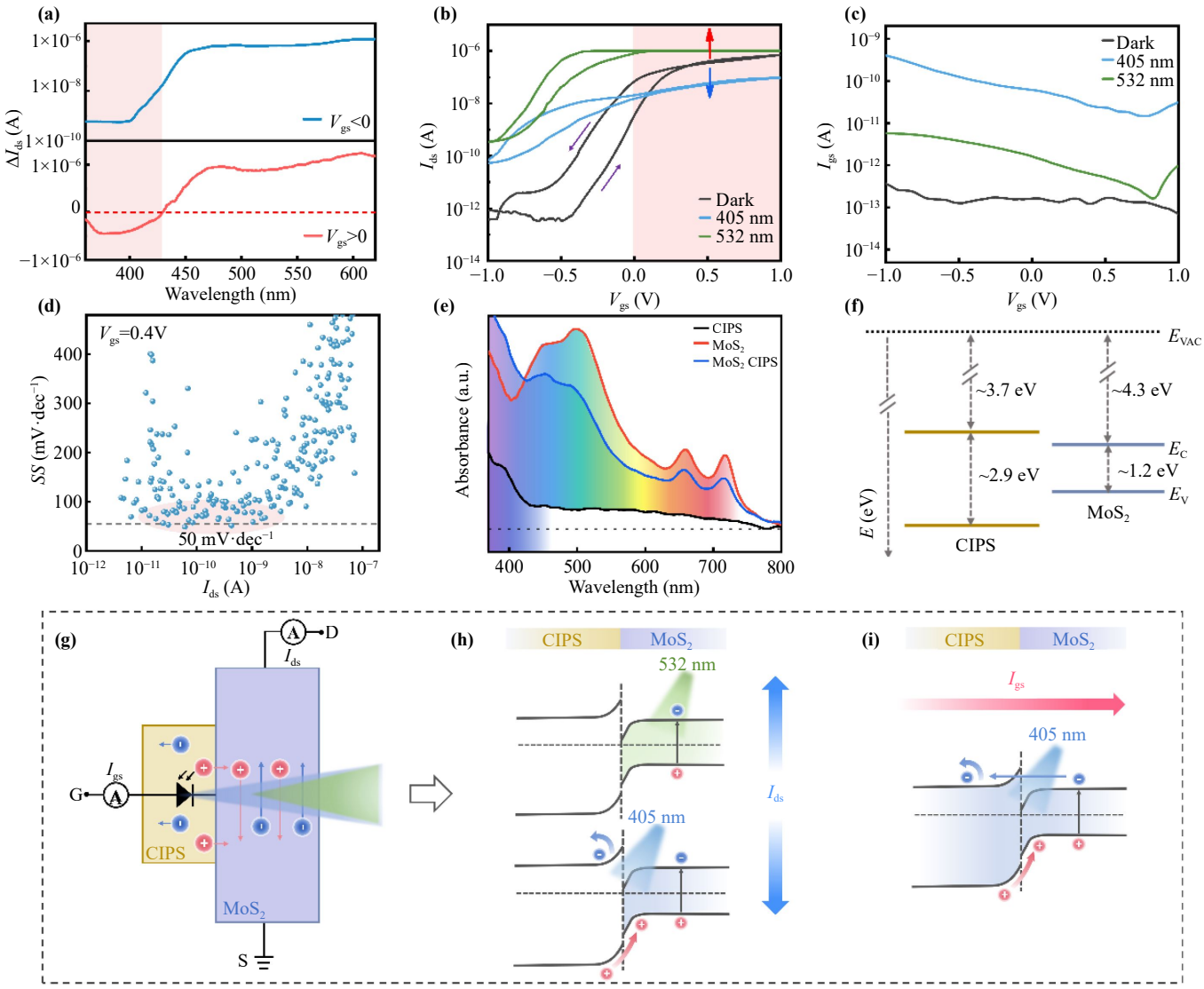


Fig. 2 Wavelength-selective dual-channel coupling mechanism. **(a)** Spectral response curves under $V_{gs} > 0$ and $V_{gs} < 0$, respectively. **(b)** I_{ds}–V_{gs} and **(c)** I_{gs}–V_{gs} transfer characteristic curves under illuminated and dark conditions. The arrows in (b) indicate the forward sweep from −1 to +1 V and the reverse sweep from +1 to −1 V, corresponding to counterclockwise hysteresis. **(d)** Subthreshold swing extracted from (b). **(e)** Absorption curves of individual CIPS and MoS_2, and the overlapping region of CIPS/MoS_2. **(f)** Energy band diagrams of CIPS and MoS_2 before contact. **(g)** Device architecture and equivalent circuit diagram. **(h)** Mechanism diagram of the I_{ds} output generated under $V_{gs} = 0$ conditions when exposed to 532 nm and 405 nm laser irradiation, respectively. **(i)** Mechanism diagram of the I_{gs} output generated under positive V_{gs} and under 405 nm laser irradiation.

bandgap of multilayer MoS_2 was adopted from the literature. Therefore, Figure 2(f) represents a schematic band alignment used to illustrate the qualitative direction of photoinduced carrier transfer. The medium-wide bandgap of CIPS enables selective optical excitation of the CIPS/MoS_2 heterojunction by 405 and 532 nm lasers. Figure 2(g) illustrates the device's photocharge transport mechanism. Under 532 nm light irradiation, since CIPS has weak absorption of visible light, the photoresponse mainly originates from MoS_2. The positive V_{gs} induces downward band bending in MoS_2, leading to electron accumulation and forming a horizontal current channel (Y_1). In contrast, CIPS exhibits strong absorption of 405 nm light, under bottom gate regulation, the photogenerated holes produced in CIPS migrate vertically toward the MoS_2 channel, forming a vertical gate current (I_{gs}) that exerts a significant inhibitory effect on the horizontal current (I_{ds}) [Figs. 2(h) and (i)]. The energy band diagrams under dark and light illumination conditions at negative gate voltage, as well as the photocurrent spectra under different gate voltages, are presented in Figs. S6 and S7, respectively. Through the

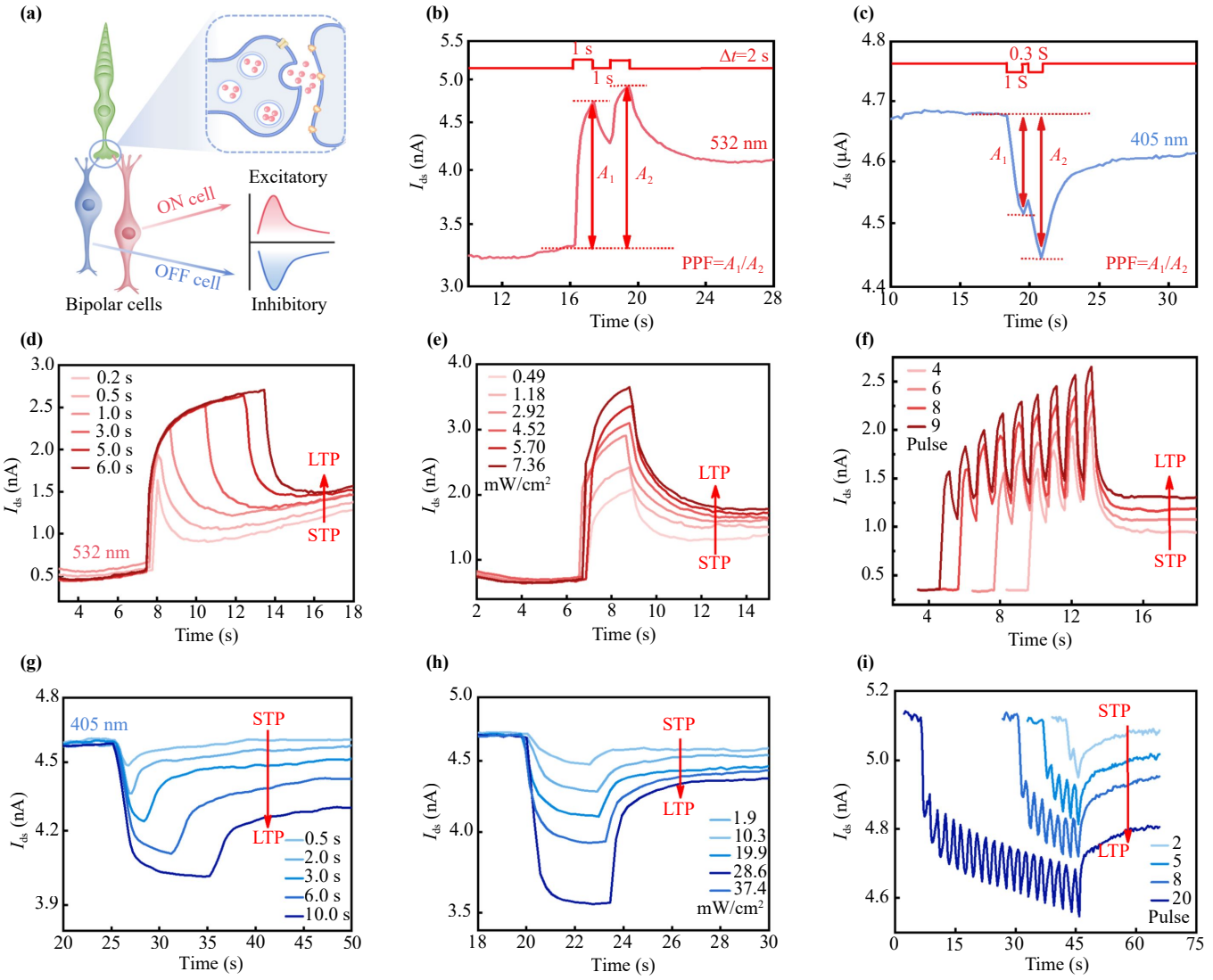


Fig. 3 Wavelength-dependent synaptic response polarity. **(a)** Schematic of bipolar cells and synapses in the retina. PPF triggered by a pair of light pulses with wavelengths of **(b)** 532 nm and **(c)** 405 nm, respectively. STP-to-LTP transition as a function of **(d)** pulse width, **(e)** intensity, and **(f)** number of 532 nm laser. STP-to-LTP transition as a function of **(g)** pulse width, **(h)** intensity, and **(i)** number of 405 nm laser pulses.

synergistic design of band engineering (CIPS/MoS_2 heterojunction) and gate control, the device achieves co-regulation of I_{ds} and I_{gs}, breaking the traditional approach in 2D devices where performance optimization is achieved by minimizing I_{gs}. In summary, Figures 2(e) and (f) can explain the output characteristics in Figs. 2(h) and (i). 532 nm light is mainly absorbed by MoS_2, which enhances I_{ds} while the I_{gs} response is relatively weak, whereas 405 nm light can also excite narrow-bandgap CIPS, enabling vertical carrier transfer and generating I_{gs} while inhibiting I_{ds}. In biological neural networks (BNNs), retinal bipolar cells are responsible for transmitting all information required for vision [42, 43]. Based on axon terminal morphology and inner plexiform layer distribution, they are classified into ON/OFF types, forming synapses with corresponding ganglion cells to relay visual signals [Fig. 3(a)]. Under light stimulation, photoreceptors reduce glutamate release, inducing depolarization of ON bipolar cells and excitatory postsynaptic currents (EPSCs), while OFF bipolar cells hyperpolarize, release inhibitory neurotransmitters, and produce inhibitory postsynaptic currents (IPSCs) [44, 45]. This mechanism, which achieves efficient detection of light intensity changes through a dynamic balance between depolarization and hyperpolarization [46, 47], provides significant insights into artificial vision sensor design. In the device, optical pulses act as presynaptic stimuli, and the resulting channel-current variation is regarded as the postsynaptic current. The positive response under 532 nm illumination corresponds to EPSC, whereas the negative response under 405 nm illumination corresponds to IPSC. The transient and

history-dependent current modulation corresponds to STP, with paired-pulse facilitation or depression serving as a representative manifestation. The enhanced and more persistent current modulation induced by increasing the pulse width, intensity, or number indicates the transition toward LTP.

Paired-pulse facilitation (PPF), a typical short-term plasticity (STP) process in biological synapses, refers to postsynaptic signal enhancement induced by successive presynaptic stimulations. Under 532 nm laser irradiation (pulse width = 1 s, pulse interval = 1 s; Fig. 3(b), the conductance enhancement induced by the second pulse is significantly higher than that induced by the first, exhibiting positive PPF behavior. This arises from incomplete electrode collection of photogenerated carriers from the first pulse, which improves the carrier injection efficiency of the second pulse. In contrast, under 405 nm laser irradiation (pulse width = 1 s, pulse interval = 0.3 s). Figure 3(c) exhibits negative PPF behavior due to the injection of photogenerated holes from CIPS into the channel. This wavelength-dependent PPF behavior not only emulates the short-term plasticity and dynamic information processing of biological synapses but also provides novel insights into developing spectrally selective photoelectric neuromorphic devices. Memory retention depends on learning intensity, duration, and frequency, repeated learning induces the STP-LTP transition, which facilitates brain information processing and storage. Human memory and forgetting are dynamically balanced, with memory mediated via synaptic potentiation and forgetting via synaptic depression. At the device level, regulating the light pulse width, intensity, and number modulates EPSC/IPSC amplitudes to achieve the STP-LTP transition, emulating memory formation and forgetting. Figures 3(d–f) show positive photoresponse behavior under 532 nm pulse irradiation, where EPSC amplitude increases long-term with pulse width, intensity, and number, mimicking long-term memory via calcium-mediated synaptic potentiation in biological synapses. In contrast, 405 nm pulses elicit negative photoresponse, with enhanced IPSC suppression as pulse parameters increase, simulating inhibitory neurotransmitter-regulated long-term forgetting [Figs. 3(g)–(i)]. Figure S8 further presents the device's emulation of color images perception, memory, and forgetting functions. The postsynaptic current variation (ΔPSC) increases with the light pulse number and decays post-stimulation [Figs. S8(a, b)], calculated as

$$\Delta PSC = I_{\text{light}} - I_{\text{dark}} . \tag{2}$$

Here, I_{dark} represents the initial current, and I_{light} denotes the current after the application of optical pulse stimulation.

As shown in Fig. S8(c), increasing the number of light pulses improves image clarity and anti-forgetting capability, while the image gradually blurs after light stimulation ceases. Benefiting from the ΔPSC differences under different light irradiations, this multi-parameter regulation mechanism lays a crucial foundation for efficient and reconfigurable neuromorphic computing.

In the retinal neural circuit, horizontal cells establish a center-surround antagonistic receptive field by forming lateral connections with multiple photoreceptor cells and bipolar cells [Fig. 4(a)]. The central region directly receives photoreceptor inputs, while the surround region integrates indirect inputs from adjacent photoreceptors via horizontal cells. This center-surround antagonistic mechanism enables parallel signal processing and lateral regulation, enhancing central contrast while suppressing the uniform background to optimize visual information processing [48, 49]. The dual-channel photosensor's I_{ds} and I_{gs} output channels mimic the direct conduction pathway of bipolar cells and the lateral modulation pathway regulated by horizontal cells, respectively. Specifically, the increase in I_{ds} under 532 nm illumination represents center excitation, whereas the activation of I_{gs} accompanied by the suppression of I_{ds} under 405 nm illumination represents surround activation and inhibitory feedback. We first measured the time-dependent current response of the photosensor under different irradiations [Figs. 4(b, c)]. Under 532 nm light, the I_{ds} channel exhibits a positive response, corresponding to ON-pathway activation in the central region of bipolar cells, while the I_{gs} channel shows a negligible response, analogous to the weak feedback of horizontal cells in the center. In contrast, 405 nm laser irradiation induces a positive I_{gs} response mimicking peripheral horizontal cell activation, as well as a negative I_{ds} response, which is analogous to horizontal cells' negative feedback regulation of bipolar cell peripheral responses via inhibitory neurotransmitters (e.g., γ-aminobutyric acid, GABA) to suppress peripheral bipolar cell activity.

Rational design of the device array enables real-time image preprocessing using wavelength-dependent positive/negative photoconductive responses. We simulated a 28 × 28 array for image denoising, with the input of a noisy image containing a green "3" pattern and blue background noise [left in Fig. 4(b)]. The target pattern area generates a positive photocurrent under 532 nm light, while 405 nm laser irradiation triggers a negative photoconductive response in the background. Furthermore, the generated dual-channel outputs ($I_{\text{ds}}/I_{\text{gs}}$) correspond to the direct pathway/lateral pathway of the retina, respectively [right in Fig. 4(b)]. Analysis of Figure 4(c) yields the quantitative correlation between pulse number and photocurrent variation (Fig. S9). Experimental results show that with an increase in the number of pulses, the Weber contrast significantly increases to up to 266.4% under 405 nm and 532 nm irradiation, thereby producing a clear target pattern [inset in Fig. 4(c)].

In addition, the denoised image preprocessed by the

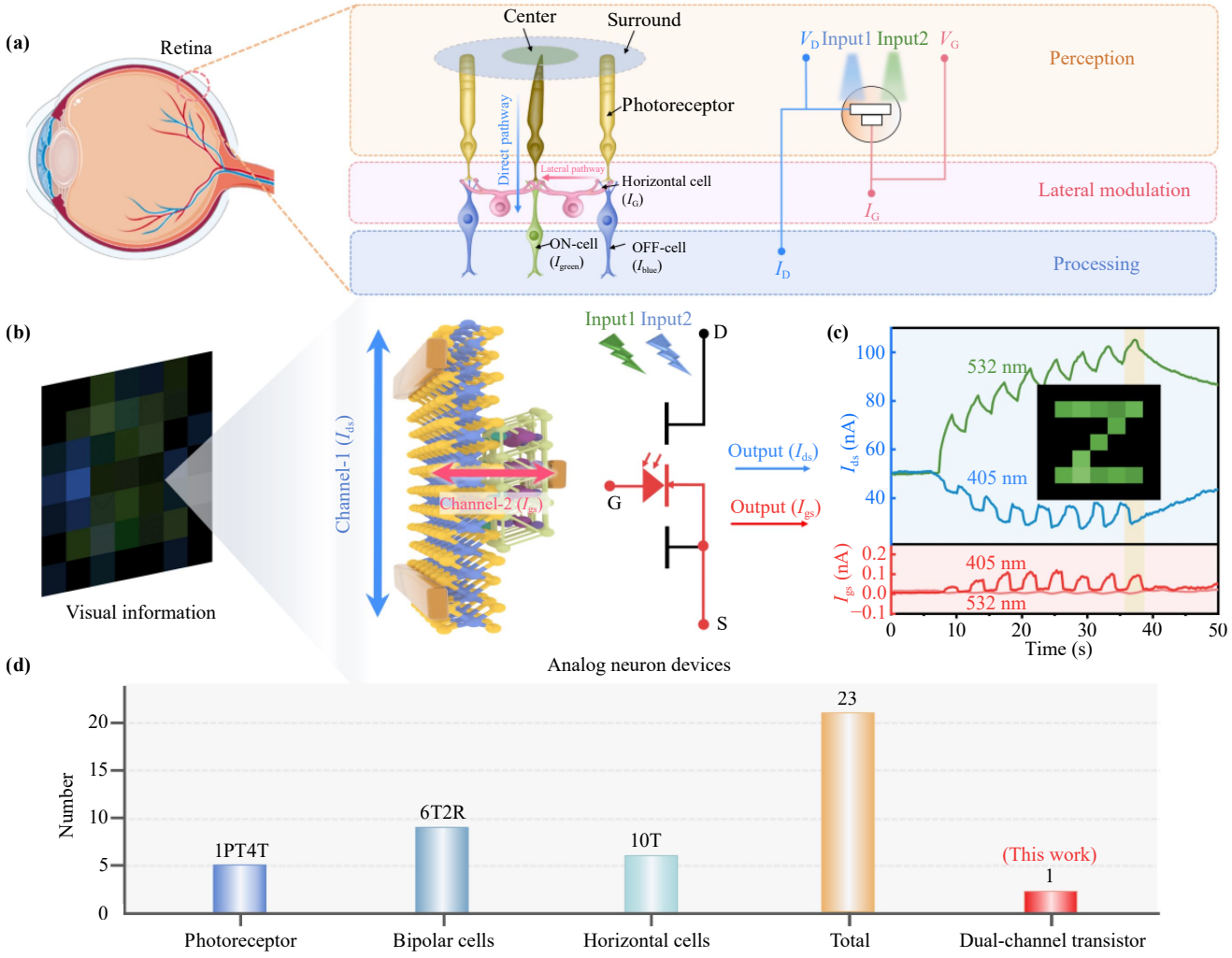
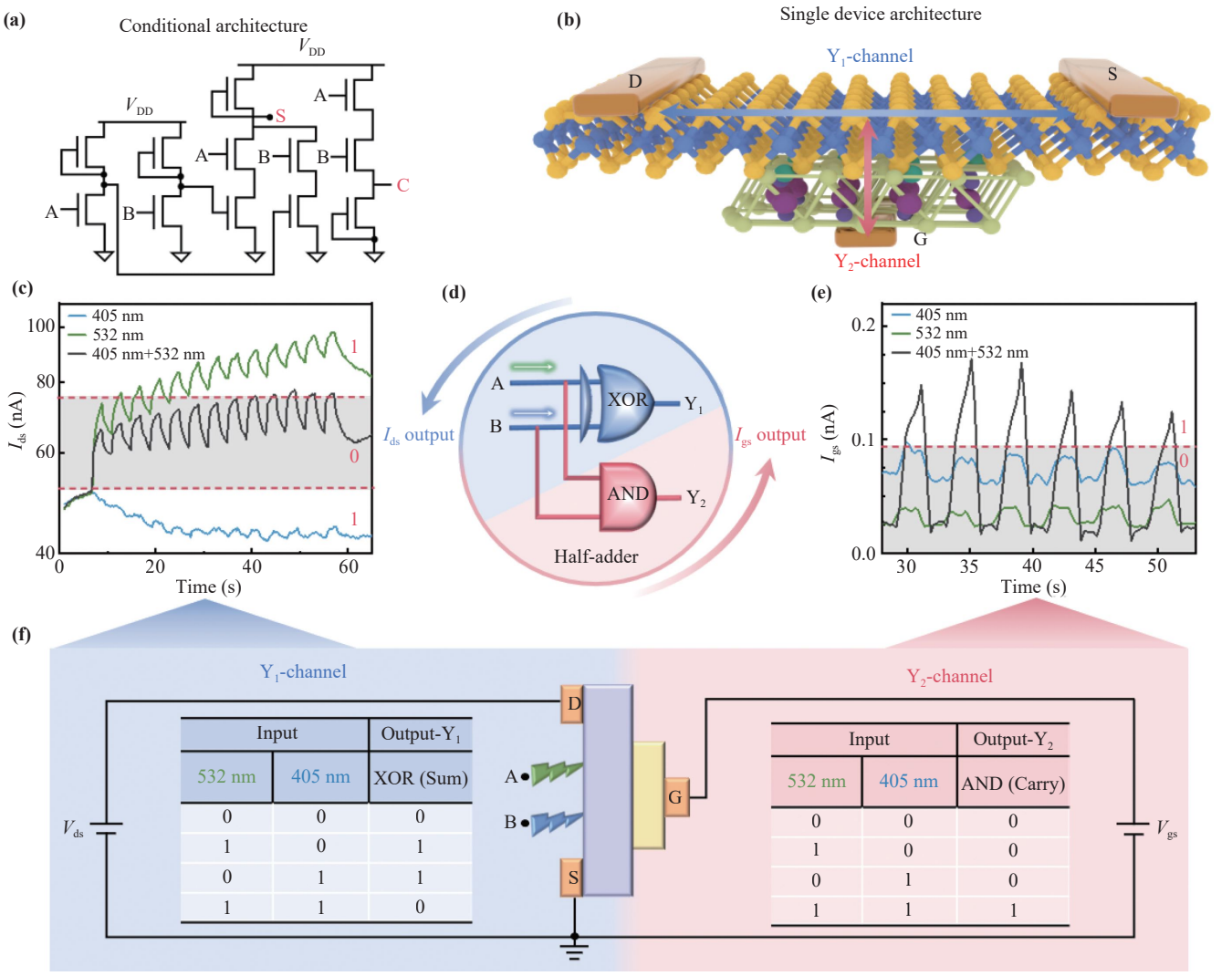


Fig. 4 Dual-channel readout enabling bio-retinal center-surround antagonism. **(a)** Center-surround antagonism replicated by I_{ds} and I_{gs}. **(b)** Noisy input image (green "3" on blue noise). **(c)** Denoised output image after device preprocessing. **(d)** Statistical chart of the number of devices used to realize each neuron in the retina under the traditional mode.

array is input into a convolutional neural network (CNN) for image recognition (Fig. S10), achieving a significantly improved accuracy of 98.4%. Therefore, the device emulates retinal visual signal preprocessing for sensor-level noise suppression and contrast enhancement. Compared with traditional retinal-mimetic designs [Fig. 4(d)], it uses the fewest transistors, a reduction of approximately 95.7% [6, 50–52]. Synergistic wavelength selectivity and dual-channel antagonistic mechanisms enable precise replication of the retina's "center-excitation, surround-inhibition" core computation, opening new avenues for 2D semiconductor applications in neuromorphic engineering and advanced intelligent image sensors. Having demonstrated the device's bio-inspired perception capability, we further exploit its programmable photoresponse to achieve digital logic, which is absent in biology. Recent studies show that a single biological neuron can perform nonlinear Boolean operations (e.g., XOR operation) [53]. However, existing neuromorphic systems usually separate logical computation from sensory simulation functions, which relies on complex hybrid circuit designs. Additionally, conventional CMOS half-adder circuits typically require at least 12 transistors to realize the logic functions [as shown in Fig. 5(a)], which not only increases power consumption but also limits high-density device integration. By contrast, based on the photosensitive dielectric gate regulation mechanism, this study designs a photosensor with both a horizontal I_{ds} channel and a vertical I_{gs} channel [Fig. 5(b)]. Through the independent control of the two channels via selective optical inputs, the logic function of an all-optical half-adder can be realized, reducing the transistor count by 91.7%, significantly lowering power consumption, and enhancing neuromorphic information processing capabilities.

As one of the most fundamental arithmetic logic units in digital circuits, the half-adder is used to perform the addition of two single-bit binary numbers. It consists of



Input		Output-Y_1
532 nm	405 nm	XOR (Sum)
0	0	0
1	0	1
0	1	1
1	1	0

Input		Output-Y_2
532 nm	405 nm	AND (Carry)
0	0	0
1	0	0
0	1	0
1	1	1

Fig. 5 Dual-channel readout enabling all-optical half-adder within a single-device. **(a)** Conventional CMOS architecture. **(b)** Schematic of the single-device architecture. **(c)** I_{ds} implements XOR (sum) and **(e)** I_{gs} implements AND (carry). **(d)** A single device implementing half-adder logic. **(f)** Equivalent circuit of the half-adder and its truth table shown in the inset.

two inputs A and B, one carry output C_0, and a sum terminal S. Specifically, the XOR logic gate is responsible for calculating the sum, while the AND logic gate is responsible for generating the carry [Fig. 5(d)]. Figures 5(c) and (e), respectively, show the I_{ds} and I_{gs} output curves of the device under both 532 nm and 405 nm light irradiation, with bias conditions set at V_{ds} = 1 V and V_{gs} = 1 V. The red dashed lines in the figures represent the threshold levels of the current response, which are used to distinguish the logic states of the device. We define the irradiation states of 532 nm and 405 nm light as the logic input signals, with the light-on state representing logic "1" and the light-off state representing logic "0". Concurrently, the responses of I_{ds} and I_{gs} are defined as the logic outputs, where a significant current response corresponds to logic "1" (positive or negative photoresponse), and a weak current response corresponds to logic "0". This experiment uses a dual-ended fiber to simultaneously illuminate the device surface with two light beams at 405 nm and 532 nm, enabling precise periodic alignment of the optical signals. The logical measurement employs a fixed timing sequence to apply both optical inputs, generating the (1,1) input state through temporal overlap of the two pulses. Results show that the transistor can implement XOR logic at the I_{ds} output and AND logic at the I_{gs} output. Figure 5(f) illustrates the equivalent circuit structure of the half-adder, and the accompanying truth table in the inset further validates the correctness of its logical functions. Additionally, the half-adder logic based on the dual-channel output photosensor enables image encryption and decryption, as shown in Fig. S11 (Supporting Information). Through a dual verification mechanism, it significantly enhances the security of image transmission and storage.

4 Conclusions

In summary, we demonstrate a dual-readout transistor employing n-type MoS_2 as the channel and CIPS as the ferro-photoactive gate dielectric. The dual readouts consist of the horizontal source-drain current I_{ds} and the vertical gate-source current I_{gs}. Through the collaborative design of wavelength selectivity and the dual-readout antagonism mechanism, real-time contrast enhancement analogous to the biological retinal mechanism is physically constructed, enabling in-sensor preprocessing of visual information. Furthermore, by leveraging the cross-modulation characteristics of the dual current channels, the logical operation of an all-optical half-adder can be simultaneously realized, which will be of great significance for the construction of high-efficiency neuromorphic systems. Future work will focus on broadening the response spectrum beyond 405/532 nm for broadband in-sensor computing.

Declarations The authors declare that they have no competing interests and there are no conflicts.

Data availability statement The data that support the findings of this study are available from the corresponding authors upon reasonable request.

Electronic supplementary materials The supporting information is available free of charge at https://journal.hep.com.cn/fop/EN/pdf/10.15302/frontphys.2027.044201. Device configuration and characterization, dielectric properties of CIPS, electrical characteristics of the dual-channel phototransistor, band diagrams and working mechanisms of the dual-channel phototransistor, emulation of the perception and preprocessing functions of the human retina, and the logical function of the all-optical half-adder.

Acknowledgements This work was supported by the National Natural Science Foundation of China (Grant Nos. 12574072, 12474067 and 12374070), the Natural Science Foundation of Henan Province (Grant No. 252300421297), the Program for Science and Technology Innovation Talents in the University of Henan Province (Grant No. 202300410221), and the Henan Province Universities Scientific Research Key Project (Grant No. 21A140015).

References

1. Y. Chai, In-sensor computing for machine vision, *Nature* 579(7797), 32 (2020)
2. G. D. Zhou, J. Li, Q. L. Song, L. D. Wang, Z. J. Ren, B. Sun, X. F. Hu, W. H. Wang, G. B. Xu, X. D. Chen, L. Cheng, F. C. Zhou, and S. K. Duan, Full hardware implementation of neuromorphic visual system based on multimodal optoelectronic resistive memory arrays for versatile image processing, *Nat. Commun.* 14(1), 8489 (2023)
3. D. Ielmini and H. S. P. Wong, In-memory computing with resistive switching devices, *Nat. Electron.* 1(6), 333 (2018)
4. A. Sebastian, M. Le Gallo, R. Khaddam-Aljameh, and E. Eleftheriou, Memory devices and applications for in-memory computing, *Nat. Nanotechnol.* 15(7), 529 (2020)
5. G. Indiveri, and R. Douglas, Neuromorphic vision sensors, *Science* 288(5469), 1189 (2000)
6. F. Y. Liao, Z. Zhou, B. J. Kim, J. W. Chen, J. L. Wang, T. Q. Wan, Y. Zhou, A. T. Hoang, C. Wang, J. F. Kang, J. H. Ahn, and Y. Chai, Bioinspired in-sensor visual adaptation for accurate perception, *Nat. Electron.* 5(2), 84 (2022)
7. P. Y. Huang, B. Y. Jiang, H. J. Chen, J. Y. Xu, K. Wang, C. Y. Zhu, X. Y. Hu, D. Li, L. Zhen, F. C. Zhou, J. K. Qin, and C. Y. Xu, Neuro-inspired optical sensor array for high-accuracy static image recognition and dynamic trace extraction, *Nat. Commun.* 14(1), 6736 (2023)
8. Y. R. Wang, S. M. Nie, S. S. Liu, Y. F. Hu, J. W. Fu, J. Y. Ming, J. Liu, Y. Q. Li, X. He, L. Wang, W. Li, M. D. Yi, H. F. Ling, L. H. Xie, and W. Huang, Dual-adaptive heterojunction synaptic transistors for efficient machine vision in harsh lighting conditions, *Adv. Mater.* 36(32), 2404160 (2024)
9. Y. K. Yang, C. Pan, Y. X. Li, X. Yang dong, P. F. Wang, Z. A. Li, S. Wang, W. T. Yu, G. Y. Liu, B. Cheng, Z. F. Di, S. J. Liang, and F. Miao, In-sensor dynamic computing for intelligent machine vision, *Nat. Electron.* 7(3), 2520 (2024)
10. S. Strauss, M. M. Korympidou, Y. L. Ran, K. Franke, T. Schubert, T. Baden, P. Berens, T. Euler, and A. L. Vlasits, Center-surround interactions underlie bipolar cell motion sensitivity in the mouse retina, *Nat. Commun.* 13(1), 5574 (2022)
11. J. A. Gaynes, S. A. Budoff, M. J. Grybko, J. B. Hunt, and A. Poleg-Polsky, Classical center-surround receptive fields facilitate novel object detection in retinal bipolar cells, *Nat. Commun.* 13(1), 5575 (2022)
12. M. H. Turner, G. W. Schwartz, and F. Rieke, Receptive field center-surround interactions mediate context-dependent spatial contrast encoding in the retina, *eLife* 7, e38841 (2018)
13. S. Y. Wang, X. X. Liu, and P. Zhou, The road for 2D semiconductors in the silicon age, *Adv. Mater.* 34(48), 2106886 (2022)
14. B. Radisavljevic, A. Radenovic, J. Brivio, V. Giacometti, and A. Kis, Single-layer MoS_2 transistors, *Nat. Nanotechnol.* 6(3), 147 (2011)
15. Y. Liu, X. D. Duan, H. J. Shin, S. Park, Y. Huang, and X. F. Duan, Promises and prospects of two-dimensional transistors, *Nature* 591(7848), 43 (2021)
16. K. S. Novoselov, A. Mishchenko, A. Carvalho, and A. H. C. Neto, 2D materials and van der Waals heterostructures, *Science* 353(6298), aac9439 (2016)
17. Z. R. Peng, L. Tong, W. H. Shi, L. L. Xu, X. Y. Huang, Z. Li, X. X. Yu, X. H. Meng, X. He, S. J. Lv, G. C. Yang, H. Hao, T. Jiang, X. S. Miao, ang L. Ye, Multifunctional human visual pathway-replicated hardware based on 2D materials, *Nat. Commun.* 15(1), 8650 (2024)

18. X. Liu, M. Huang, X. F. Zou, W. Ali, S. U. Rehman, J. Li, Z. W. Li, L. Xiang, and A. L. Pan, Alcohol-sensitive MoS_2 optoelectronic synapses for mimicking human-like visual adaptation, *InfoMat* 7(8), e70019 (2025)
19. Y. Deng, S. H. Liu, M. S. Li, N. Zhang, Y. M. Feng, J. B. Han, Y. Kapitonov, Y. Li, and T. Y. Zhai, Large-area growth of synaptic heterostructure arrays for integrated neuromorphic visual perception chips, *Chip* 3(2), 100088 (2024)
20. K. T. Zhang, Z. W. Huo, Y. F. Wang, H. Yan, J. R. Yu, L. Q. Cheng, Y. X. Fu, C. Liu, Z. H. Li, Z. Liu, Z. L. Wang, Q. J. Sun, and X. D. Lin, Neuromorphic tactile-visual perception based on 2D ReS_2/CIPS heterojunction artificial synapse, *Nano Energ.* 144, 111399 (2025)
21. Y. Q. Liu, Y. H. Wu, H. J. Han, Y. Wang, R. X. Peng, K. Liu, D. Yi, C. W. Nan, and J. Ma, $CuInP_2S_6$-based electronic/optoelectronic synapse for artificial visual system application, *Adv. Funct. Mater.* 34(1), 2306945 (2023)
22. Z. Y. Lin, Y. Liu, U. Halim, M. N. Ding, Y. Y. Liu, Y. L. Wang, C. C. Jia, P. Chen, X. D. Duan, C. Wang, F. Song, M. F. Li, C. Z. Wan, Y. Huang, and X. F. Duan, Solution-processable 2D semiconductors for high-performance large-area electronics, *Nature* 562(7726), 254 (2018)
23. X. X. Sun, C. G. Zhu, J. L. Yi, L. Xiang, C. Ma, H. W. Liu, B. Y. Zheng, Y. Liu, W. X. You, W. J. Zhang, D. L. Liang, Q. Shuai, X. L. Zhu, H. G. Duan, L. Liao, Y. Liu, D. Li, and A. L. Pan, Reconfigurable logic-in-memory architectures based on a two-dimensional van der Waals heterostructure device, *Nat. Electron.* 5(11), 752 (2022)
24. K. K. Gao, B. Sun, Z. L. Cao, X. G. Duan, W. T. Yan, G. Q. Tong, G. D. Zhou, X. L. Chen, and J. Y. Shao, Biomaterial/organic heterojunction based memristor for logic gate circuit design, data encryption, and image reconstruction, *Adv. Funct. Mater.* 34(36), 2401132 (2024)
25. X. P. Li, Z. J. Wang, X. J. Tang, P. Z. Yuan, L. Li, C. H. Shen, Y. R. Jiang, X. H. Song, and C. X. Xia, Logic computing field-effect transistors based on a monolayer WSe_2 homojunction for the semi-adder and decoder, *Nano Lett.* 24(35), 11132 (2024)
26. Z. D. Luo, S. Q. Zhang, Y. Liu, D. W. Zhang, X. T. Gan, J. Seidel, Y. Liu, G. Q. Han, M. Alexe, and Y. Hao, Dual-ferroelectric-coupling-engineered two-dimensional transistors for multifunctional in-memory computing, *ACS Nano* 16(2), 3362 (2022)
27. H. W. Chen, X. Y. Xue, C. S. Liu, J. B. Fang, Z. Wang, J. L. Wang, D. W. Zhang, W. D. Hu, and P. Zhou, Logic gates based on neuristors made from two-dimensional materials, *Nat. Electron.* 4(6), 399 (2021)
28. J. J. Nassi and E. M. Callaway, Parallel processing strategies of the primate visual system, *Nat. Rev. Neurosci.* 10(5), 360 (2009)
29. R. H. Masland, The neuronal organization of the retina, *Neuron* 76(2), 266 (2012)
30. B. R. Conway, Color vision, cones, and color-coding in the cortex, *Neuroscientist* 15(3), 274 (2009)
31. J. I. Toyoda and K. Tonosaki, Effect of polarisation of horizontal cells on the on-centre bipolar cell of carp retina, *Nature* 276(5686), 399 (1978)
32. H. Qian and J. E. Dowling, Novel GABA responses from rod-driven retinal horizontal cells, *Nature* 361(6408), 162 (1993)
33. W. K. Stell, A. T. Ishida, and D. O. Lightfoot, Structural basis for on-and off-center responses in retinal bipolar cells, *Science* 198(4323), 1269 (1977)
34. J. E. Dowling, J. E. Brown, and D. Major, Synapses of horizontal cells in rabbit and cat retinas, *Science* 153(3744), 1639 (1966)
35. F. C. Liu, L. You, K. L. Seyler, X. B. Li, P. Yu, et al., Room-temperature ferroelectricity in $CuInP_2S_6$ ultrathin flakes, *Nat. Commun.* 7(1), 12357 (2016)
36. H. Li, Q. Zhang, C. C. R. Yap, B. K. Tay, T. H. T. Edwin, A. Olivier, and D. Baillargeat, From bulk to monolayer MoS_2, *Adv. Funct. Mater.* 22(7), 1385 (2012)
37. X. W. Wang, P. Yu, Z. D. Lei, C. Zhu, X. Cao, F. C. Liu, L. You, Q. S. Zeng, Y. Deng, C. Zhu, J. D. Zhou, Q. D. Fu, J. L. Wang, Y. Z. Huang, and Z. Liu, Van der Waals negative capacitance transistors, *Nat. Commun.* 10, 3037 (2019)
38. D. Daw, H. Bouzid, M. Jung, D. Suh, C. Biswas, and Y. Hee Lee, Ultrafast negative capacitance transition for 2D ferroelectric MoS_2/graphene transistor, *Adv. Mater.* 36(13), 2304338 (2024)
39. H. Chen, Y. F. Long, S. Y. Zhang, K. Liu, M. F. Chen, J. X. Zhao, M. W. Si, and L. Wang, Van der Waals ferroelectric $CuCrP_2S_6$-enabled hysteresis-free negative capacitance field-effect transistors, *Adv. Mater.* 37(18), 2419125 (2025)
40. J. B. Wu, H. Y. Chen, N. Yang, J. Cao, X. D. Yan, F. X. Liu, Q. B. Sun, X. Ling, J. Guo, and H. Wang, High tunnelling electroresistance in a ferroelectric van der Waals heterojunction via giant barrier height modulation, *Nat. Electron.* 3(8), 466 (2020)
41. A. P. Nayak, S. Bhattacharyya, J. Zhu, J. Liu, X. Wu, T. Pandey, C. Q. Jin, A. K. Singh, D. Akinwande, and J. F. Lin, Pressure-induced semiconducting to metallic transition in multilayered molybdenum disulphide, *Nat. Commun.* 5(3731), 3731 (2014)
42. T. Euler, S. Haverkamp, T. Schubert, and T. Baden, Retinal bipolar cells: elementary building blocks of vision, *Nat. Rev. Neurosci.* 15(8), 507 (2014)
43. J. C. Hsiang, N. Shen, F. Soto, and D. Kerschensteiner, Distributed feature representations of natural stimuli across parallel retinal pathways, *Nat. Commun.* 15(1), 1920 (2024)
44. H. M. Schreyer and T. Gollisch, Nonlinear spatial integration in retinal bipolar cells shapes the encoding of artificial and natural stimuli, *Neuron* 109(10), 1692 (2021)
45. S. H. DeVries, Bipolar cells use Kainate and AMPA receptors to filter visual information into separate channels, *Neuron* 28(3), 847 (2000)
46. Q. L. Lin, C. Q. Li, H. G. Xiong, M. Zhang, J. W. Qiao, J. P. Wu, L. Yang, S. Wang, H. Chen, Y. N. Wei, D. Zheng, G. H. Lu, X. T. Hao, D. H. Yu, Y. H. Cai, A. Facchetti, and H. Huang, Event-driven retinomorphic photodiode with bio-plausible temporal dynamics, *Nat. Nanotechnol.* 20(9), 1213 (2025)

47. Z. Han, Y. C. Zhang, Q. Mi, J. You, N. N. Zhang, Z. Y. Zhong, Z. M. Jiang, H. Guo, H. Y. Hu, L. M. Wang, and Z. M. Zhu, Reconfigurable homojunction phototransistor for near-zero power consumption artificial biomimetic retina function, *ACS Nano* 18(43), 29968 (2024)
48. S. Strauss, M. M. Korympidou, Y. L. Ran, K. Franke, T. Schubert, T. Baden, P. Berens, T. Euler, and A. L. Vlasits, Center-surround interactions underlie bipolar cell motion sensitivity in the mouse retina, *Nat. Commun.* 13(1), 5574 (2022)
49. R. M. Balboa, and N. M. Grzywacz, The role of early retinal lateral inhibition: More than maximizing luminance information, *Vis. Neurosci.* 17(1), 77 (2000)
50. X. Q. Li, L. Yi, X. M. Yin, J. F. Cheng, Q. Xin, and A. M. Song, Fully screen-printed paper-based ZnO synaptic transistor arrays for visual perception and neuromorphic computing, *npj Flexible Electron.* 9(1), 57 (2025)
51. C. Y. Wang, S. J. Liang, S. Wang, P. F. Wang, Z. Li, Z. R. Wang, A. Y. Gao, C. Pan, C. Liu, J. Liu, et al, Gate-tunable van der Waals heterostructure for reconfigurable neural network vision sensor, *Sci. Adv.* 6(26), eaba6173 (2020)
52. X. Wan, T. Tsuruoka, and K. Terabe, Neuromorphic system for edge information encoding: Emulating retinal center-surround antagonism by Li-ion-mediated highly interactive devices, *Nano Lett.* 21(19), 7938 (2021)
53. A. Gidon, T. A. Zolnik, P. Fidzinski, F. Bolduan, A. Papoutsi, P. Poirazi, M. Holtkamp, I. Vida, and M. E. Larkum, Dendritic action potentials and computation in human layer 2/3 cortical neurons, *Science* 367(6473), 83 (2020)